HHS Public Access

Author manuscript

*Magn Reson Med*. Author manuscript; available in PMC 2017 January 01.

Published in final edited form as:

*Magn Reson Med*. 2016 January ; 75(1): 137–149. doi:10.1002/mrm.25581.

# Quantitative Assessment of Amide Proton Transfer (APT) and Nuclear Overhauser Enhancement (NOE) Imaging with Extrapolated Semi-solid Magnetization Transfer Reference (EMR) Signals: Application to a Rat Glioma Model at 4.7 T

**Hye-Young Heo**[1], **Yi Zhang**[1], **Dong-Hoon Lee**[1], **Xiaohua Hong**[1], and **Jinyuan Zhou**[1,2,*]

[1]Divison of MR Research, Department of Radiology, Johns Hopkins University School of Medicine, Baltimore, Maryland, USA

[2]F.M. Kirby Research Center for Functional Brain Imaging, Kennedy Krieger Institute, Baltimore, Maryland, USA

## Abstract

**Purpose—**To quantify APT and NOE contributions to *in vivo* chemical exchange saturation transfer MRI signals in tumors.

**Theory and Methods—**Two-pool (free water and semi-solid protons) and four-pool (free water, semi-solid, amide, and upfield NOE-related protons) tissue models combined with the super-Lorentzian lineshape for semi-solid protons were used to fit wide and narrow frequency-offset magnetization-transfer (MT) data, respectively. Extrapolated semi-solid MT signals at 3.5 and −3.5 ppm from water were used as reference signals to quantify APT and NOE, respectively. Six glioma-bearing rats were scanned at 4.7 T. Quantitative APT and NOE signals were compared at three saturation power levels.

**Results—**The observed APT signals were significantly higher in the tumor (center and rim) than in the contralateral normal brain tissue at all saturation powers, and were the major contributor to the APT-weighted image contrast (based on MT asymmetry analysis) between the tumor and the normal brain tissue. The NOE (a positive confounding factor) enhanced this APT-weighted image contrast. The fitted amide pool sizes were significantly larger, while the NOE-related pool sizes were significantly smaller in the tumor than in the normal brain tissue.

**Conclusion—**The EMR provides a relatively accurate approach for quantitatively measuring pure APT and NOE signals.

### Keywords

MT; CEST; APT; NOE; brain tumor

Corresponding and Reprint Author: Dr. Jinyuan Zhou, Division of MR Research, Department of Radiology, Johns Hopkins University School of Medicine, 600 N. Wolfe Street, Park 336, Baltimore, MD 21287, USA Phone: (+1-410) 955-7491, Fax: (+1-410) 614-1977, jzhou@mri.jhu.edu.

SUPPORTING INFORMATION

Additional Supporting Information may be found in the online version of this article.

## INTRODUCTION

Chemical exchange saturation transfer (CEST) imaging is an important molecular MRI technique that can generate contrast based on the proton exchange between bulk water protons and solute labile protons, or water protons bound to the solute (1–5). Using CEST MRI, endogenous low-concentration biomolecules with water-exchangeable labile protons (6–10); exogenous-specific molecular imaging agents (11–15); as well as tissue physico-chemical properties, such as pH (16) and temperature (17), can be sensitively detected indirectly through the bulk water signal used for clinical imaging. Notably, amide proton transfer (APT) imaging, a variant of CEST MRI, is sensitive to the interaction between water protons and amide protons (−NH) in the peptide bonds of mobile proteins and peptides in tissue (6, 16). The proton transfer ratio for the amide protons (APTR), with respect to the water signal intensity, can be quantified by (18):

$$APTR=\frac{\alpha\cdot k_{sw}\cdot[\,amide\ protons]}{(R_{1w}+k_{ws})\,[\,water\ protons]}\left(1-e^{-(R_{1w}+k_{ws})t_{sat}}\right) \quad [1]$$

where $\alpha$ is the radiofrequency (RF) saturation efficiency, $k_{ws}$ and $k_{sw}$ are the proton exchange rates (that depend on tissue pH (19)) from the free water proton pool (w) to the amide proton pool (s) and vice versa, $R_{1w}$ is the longitudinal relaxation rate of water, square brackets ([…]) denote the concentration, and $t_{sat}$ is the length of the saturation time. Thus, APT imaging has been exploited to image tissue acidosis due to acute cerebral ischemia in animals and humans (20–23). Moreover, APT has been proposed as a means to detect malignant gliomas (24–27) and other cancers (28–30), as well as to differentiate radiation necrosis from active tumors (31–33). An increased APT signal in tumors may be attributable to increased saturation transfer due to the relatively large mobile cellular protein and peptide content ([amide protons]) and some other factors (34).

Technically, CEST imaging utilizes selective RF irradiation to saturate water-exchangeable solute labile protons. However, the RF irradiation to saturate the labile protons may induce direct water saturation (DS) and conventional magnetization transfer (MT) from semi-solid macromolecules, thus complicating the CEST measurement. The mixed CEST, DS, and conventional MT effects are usually displayed in a Z-spectrum (water saturation, $S_{sat}/S_0$, as a function of transmitter frequency offset relative to water, where $S_{sat}$ and $S_0$ are the imaging signal intensities measured with and without RF saturation, respectively). To remove the contamination from the DS and conventional MT effects, magnetization transfer ratio ($MTR = 1 - S_{sat}/S_0$) asymmetry analysis has been introduced. For APT imaging, the APT-weighted (APTw) signal is thus obtained by subtracting the MTR at −3.5 ppm upfield, with respect to water, from that at +3.5 ppm (16):

$$\begin{aligned} MTR_{asym}(3.5ppm)&=\mathrm{MTR}(+3.5ppm,\mathrm{label})-\mathrm{MTR}(-3.5ppm,\mathrm{reference})\\ &=\frac{S_{sat}(-3.5ppm,\mathrm{reference})-S_{sat}(+3.5ppm,\mathrm{label})}{S_0(\mathrm{control})}\\ &=Z(-3.5ppm,\mathrm{reference})-Z(+3.5ppm,\mathrm{label}) \end{aligned} \quad [2]$$

However, the presence of the confounding nuclear Overhauser enhancement (NOE) effect in the saturated image acquired at −3.5ppm upfield, namely, $S_{sat}(-3.5ppm)$, has complicated

the interpretation of the APTw signal quantified using MTR asymmetry analysis (Eq. [2]) (24). The NOE has been highly useful in NMR spectroscopy and has recently attracted much attention in the field of CEST imaging (4, 8, 35–40). Note that the NOE and chemical exchange are also two important conventional semi-solid MT pathways (41, 42).

Several alternative image analysis (namely, non-MTR asymmetry analysis (36, 39, 43–46)) and acquisition methods (47, 48) have been introduced to measure APT and NOE signal contributions. For example, Jin et al. (36) used the average of two boundary images acquired at 3 and 4 ppm to estimate the reference image for $APT^{*}$, and that at −2 and −5 ppm to estimate the reference image for $NOE^{*}$ (the three-offset method). Zaiss et al. (43) and Desmond et al. (39) used a sum of multiple Lorentzian shapes, each with a specific amplitude, width, and frequency offset, to analyze CEST spectra. Although promising, these approximate methods are obviously limited to where the CEST and NOE dips can be well defined in the Z-spectrum, typically at a high $B_0$ magnetic field (>7 T) or at a low saturation power level (<1 μT). Jones et al. (44) also used the fitted Lorentzian lineshape to estimate the APT and NOE reference signals in low-power pulsed CEST experiments, with negligible conventional MT effects. However, the use of very low RF power (~0.5 μT) may not be optimal for APT imaging. Therefore, a new method with which to more accurately measure APT and NOE signals *in vivo* is essential.

In this study, we investigated the mixed effects of conventional MT, APT, and NOE using a fitting approach with a multiple-pool proton exchange model, and quantified the APT and NOE signals using extrapolated semi-solid MT reference (EMR) signals. We took a rat tumor model at 4.7 T as an example. Three sets of Z-spectra with different offset ranges were acquired and analyzed. The quantitative APT ($APT^{\#}$) and NOE ($NOE^{\#}$) maps, calculated by our new approach, were compared with the commonly used $MTR_{asym}$ and several quantitative multi-parametric MRI maps in the tumor-bearing rat brain. The dependence of $APT^{\#}$ and $NOE^{\#}$ on the RF saturation power was also investigated.

## THEORY

### General Consideration

Many recent CEST studies have clearly showed that the Z-spectra in tissues have multiple CEST and NOE peaks (35–40), and the center of the Z-spectra is shifted slightly upfield from the water signal (49, 50), causing a negative background signal for asymmetry analysis of Z-spectrum (24). Biological tissues may consist of various molecules with multiple mobility ranges: semi-solid ($T_2$ ~ 10 μs), mobile ($T_2$ ~ 10 ms), and relatively less mobile ($T_2$ ~ 0.1–1 ms; namely, between semi-solid and mobile). It is important to note that only mobile biomolecules can result in a well-defined APT and NOE signals in the Z-spectrum, and that these relatively mobile biomolecules are associated with a large direct saturation width of up to tens of ppm (51). The observed conventional MT asymmetry around the water signal can be understood by two equivalent hypotheses:

$$\begin{aligned} Biomolecules &= (semi-solid + relatively\ less\ mobile) + mobile \rightarrow Conventional\ MT\ is\ asymmetric \\ &= semi-solid + (relativly\ less\ mobile + mobile) \rightarrow Conventional\ MT\ is\ symmetric \end{aligned}$$

The first one assumes that the conventional semi-solid MT effect is asymmetric, a phenomenon that results from the chemical shift center mis-match between bulk water and semi-solid macromolecules in tissue (50). This essentially assumes that some relatively less mobile biomolecules are included in the "semi-solid" MT pool. The second assumes that the conventional semi-solid MT effect is symmetric, due to the fact that true semi-solid protons have an extremely large direct RF saturation width. Then, the upfield NOE effects of aliphatic and olefinic protons of relatively less mobile biomolecules apparently shift the center of the Z-spectrum, leading to the asymmetry of the observed Z-spectrum (51). This current study is based on the second assumption, and further adds mobile and relatively less mobile biomolecules to be a single NOE-related pool.

## Conventional MT Model

The theoretical description of the conventional MT effect in tissue has been well established using a two-pool model based on the modified Bloch equations, in which the free bulk water proton pool (*w*) is coupled to the semi-solid macromolecular proton pool (*m*) through magnetization exchange (52, 53). Henkelman et al. (52, 53) have derived a mathematical expression for the steady-state longitudinal magnetization of the free pool $M_z^w$, which has the equilibrium magnetization $M_0^w$:

$$\frac{M_z^w}{M_0^w}=\frac{\frac{1}{T_{1m}}\left(RM_0^mT_{1w}\right)+R_{rfm}+\frac{1}{T_{1m}}+R}{\left(RM_0^mT_{1w}\right)\left(R_{rfm}+\frac{1}{T_{1m}}\right)+\left[1+\left(\frac{\omega_1}{2\pi\Delta}\right)^2\left(\frac{T_{1w}}{T_{2w}}\right)\right]\left(R_{rfm}+\frac{1}{T_{1m}}+R\right)} \quad [3]$$

where *R* is the fundamental rate constant describing the magnetization exchange between the two proton pools; $T_{1w}$ and $T_{2w}$ are the longitudinal and transverse relaxation times of the free water proton pool, respectively; $T_{1m}$ and $T_{2m}$ are the longitudinal and transverse relaxation times of the semi-solid macromolecular proton pool, respectively; and $M_0^m$ is the fully-relaxed equilibrium magnetization value associated with the semi-solid macromolecular pool. The RF absorption rate, $R_{rfm}$, is the loss rate of the longitudinal magnetization by the semi-solid pool due to the off-resonance RF irradiation of amplitude $\omega_1$ and frequency offset Δ. The RF absorption rate is dependent on the absorption lineshape, $g_m(2\pi\Delta)$, through the relationship $R_{rfm}=\omega_1^2\pi g_m(2\pi\Delta)$. In the MT model description for tissue, a super-Lorentzian lineshape for the semi-solid macromolecular protons has been shown to be more suitable than a Lorentzian or Gaussian lineshape (54, 55):

$$g_m(2\pi\Delta)=\int_0^{\pi/2}d\theta\sin\theta\sqrt{\frac{2}{\pi}}\frac{T_{2m}}{(3cos^2\theta-1)}e^{-2\left(\frac{2\pi\Delta T_{2m}}{3cos^2\theta-1}\right)^2} \quad [4]$$

The conventional MT signal expression described by Eq. [3] can be uniquely determined in terms of five combined model parameters (52, 53), namely, *R*, $T_{1m}$, $T_{2m}$, $RM_0^mT_{1w}$, and $T_{1w}/T_{2w}$. The parameter $T_{2m}$ is included in the absorption rate $R_{rfm}$, as described above in Eq. [4]. These five model parameters can be obtained by fitting the observed MT signal to the reduced MT expression, and EMR spectra ($Z_{EMR}$) can then be obtained with the corresponding $\omega_1$ and the offset range Δ.

The relationship between the water longitudinal relaxation times without ($T_{1w}$) and with ( $T_{1w}^{obs}$, namely, experimentally observed) the effect of the semi-solid pool can be described using the following expression (52, 56):

$$T_{1w}=T_{1w}^{obs}\left[1+\left(\frac{RM_0^mT_{1w}\left(\frac{1}{T_{1m}}-\frac{1}{T_{1w}^{obs}}\right)}{\left(\frac{1}{T_{1m}}-\frac{1}{T_{1w}^{obs}}\right)+R}\right)\right] \quad [5]$$

Therefore, the independent measurement of $T_{1w}^{obs}$ from a simple inversion recovery MRI experiment allows the longitudinal and transverse relaxation times ($T_{1w}$ and $T_{2w}$) of the bulk water pool, and the fully relaxed equilibrium magnetization ( $M_0^m$) associated with the semi-solid macromolecular pool, to be uniquely determined. These parameters can be incorporated into the four-pool model as prior known information, reducing the over-fitting errors.

## Four-Pool APT and NOE Model

APT imaging can be described well by the modified Bloch equations with exchange terms (18, 37, 45, 57–60). To describe the *in vivo* proton exchange processes between the free water proton pool ($w$), the semi-solid macromolecular proton pool ($m$), the amide proton pool of mobile proteins and peptides ($s_1$), as well as the upfield NOE-related proton pool ($s_2$), a three- or four-pool exchange model is needed (37, 45). Assuming that the amount of exchange between three relatively small pools $m$, $s_1$, and $s_2$, compared with the amount of exchange with free water protons, is negligible, the magnetization in each pool ( $M_{x,y,z}^i$, $i$ = $w$, $s_1$, $s_2$, $m$) in the presence of exchange and RF irradiation can be described as follows:

$$dM_x^w/dt=-k_{2w}M_x^w+k_{s_1w}M_x^{s_1}+k_{s_2w}M_x^{s_2}+k_{mw}M_x^m-(\omega_w-\omega)\,M_y^w \quad [6]$$

$$dM_x^{s_1}/dt=k_{ws_1}M_x^w-k_{2s_1}M_x^{s_1}-(\omega_{s_1}-\omega)\;M_y^{s_1} \quad [7]$$

$$dM_x^{S_2}/dt=k_{ws_2}M_x^w-k_{2s_2}M_x^{s_2}-(\omega_{s_2}-\omega)\;M_y^{s_2} \quad [8]$$

$$dM_x^m/dt=k_{wm}M_x^w-k_{2m}M_x^m-(\omega_m-\omega)\;M_y^m \quad [9]$$

$$dM_y^w/dt=(\omega_w-\omega)\;M_x^w-k_{2w}M_y^w+k_{s_1w}M_y^{s_1}+k_{s_2w}M_y^{s_2}+k_{mw}M_y^m-\omega_1M_z^w \quad [10]$$

$$dM_y^{s_1}/dt=(\omega_{s_1}-\omega)\;M_x^{s_1}+k_{ws_1}M_y^w-k_{2s_1}M_y^{s_1}-\omega_1M_z^{s_1} \quad [11]$$

$$dM_y^{s_2}/dt=(\omega_{s_2}-\omega)\;M_x^{s_2}+k_{ws_2}M_y^w-k_{2s_2}M_y^{s_2}-\omega_1M_z^{s_2} \quad [12]$$

$$dM_y^m/dt=(\omega_m-\omega)\ M_x^m+k_{wm}M_y^w-k_{2m}M_y^m-\omega_1 M_z^m \quad [13]$$

$$dM_z^w/dt=\omega_1 M_y^w-k_{1w}M_z^w+k_{s_1w}M_z^{s_1}+k_{s_2w}M_z^{s_2}+k_{mw}M_z^m+M_0^w/T_{1w} \quad [14]$$

$$dM_z^{s_1}/dt=\omega_1 M_y^{s_1}+k_{ws_1}M_z^w-k_{1s_1}M_z^{s_1}+M_0^{s_1}/T_{1s_1} \quad [15]$$

$$dM_z^{s_2}/dt=\omega_1 M_y^{s_2}+k_{ws_2}M_z^w-k_{1s_2}M_z^{s_2}+M_0^{s_2}/T_{1s_2} \quad [16]$$

$$dM_z^m/dt=\omega_1 M_y^m+k_{wm}M_z^w-k_{1m}M_z^m+M_0^m/T_{1m} \quad [17]$$

$$k_{1w}=1/T_{1w}+k_{ws_1}+k_{ws_2}+k_{wm} \quad [18]$$

$$k_{1s_1}=1/T_{1s_1}+k_{s_1w} \quad [19]$$

$$k_{1s_2}=1/T_{1s_2}+k_{s_2w} \quad [20]$$

$$k_{1m}=1/T_{1m}+k_{mw} \quad [21]$$

$$k_{2w}=1/T_{2w}+k_{ws_1}+k_{ws_2}+k_{wm} \quad [22]$$

$$k_{2s_1}=1/T_{2s_1}+k_{s_1w} \quad [23]$$

$$k_{2s_2}=1/T_{2s_2}+k_{s_2w} \quad [24]$$

$$k_{2m}=1/T_{2m}+k_{mw} \quad [25]$$

where $k_{ij}$ represents the proton exchange rate from pool *i* to pool *j;* $T_{1i}$ and $T_{2i}$ are the longitudinal and transverse relaxation times of pool *i*, respectively; $\omega_1$ is the RF saturation amplitude; $\omega$ is the RF saturation frequency; $\omega_i$ is the resonance frequency of pool *i*; and $M_0^i$ is the equilibrium magnetization of pool *i.* The lineshape of pool *m* can be obtained from Eq. [9] and Eq. [13] by assuming a steady-state condition and excluding the transverse exchange terms of pool:

$$M_y^m=-\frac{\omega_1 T_{2m}M_z^m}{1+T_{2m}^2(\omega_m-\omega)^2} \quad [26]$$

Inserting Eq. [26] into Eq. [17], we obtain:

$$dM_z^m/dt = k_{wm}M_z^w - (k_{1m}+R_{rfm})M_z^m + M_0^m/T_{1m} \quad [27]$$

Finally, the four-pool model can be built by replacing Eq. [17] with Eq. [27] (using the super-Lorentzian lineshape) to model the MT effect of macromolecular protons. The 10-dimensional coupled linear differential equations can be rewritten in a matrix form as:

$$\frac{dM}{dt} = AM + B \quad [28]$$

The analytical solution of Eq. [28] is:

$$M = \left(M_0 + \frac{B}{A}\right)e^{At} - \frac{B}{A} \quad [29]$$

## APTw Imaging Signal and Contrast

For APT imaging, under zero-order approximation, one has (16):

$$\begin{aligned} MTR_{asym}(3.5ppm) &= APTR + MTR'_{asym}(3.5ppm) \\ &\approx APTR - [NOER^{mobile}(-3.5ppm) + NOER^{relativly\ mobile}(-3.5ppm)] \\ &= APTR - NOER(-3.5ppm) \end{aligned} \quad [30]$$

where $MTR'_{\mathrm{asym}}$ is dominated by the upfield intramolecular and intermolecular NOE effects of various polypeptides, lipids, and metabolites in tissue, continuously distributed from mobile to semi-solid, which can assumingly be quantified by two NOE-based MT ratios with different origins ($NOER = NOER^{mobile} + NOE^{relatively\ mobile}$). The latter component, originated from those relatively mobile biomolecules, was previously thought to be the inherent $MTR_{\mathrm{asym}}$ of the semi-solid conventional MT effect (24, 50). The $\mathrm{MTR_{asym}}(3.5\mathrm{ppm})$ images calculated by Eq. [30] are usually called APTw images (24). Further, the APTw image contrast between tumor and contralateral brain tissue can be described by (51):

$$\begin{aligned} \Delta MTR_{asym}(3.5ppm) &= [MTR_{asym}(3.5ppm)]^{tumor} - [MTR_{asym}(3.5ppm)]^{normal} \\ &= [APTR^{tumor} - APTR^{normal}] + [NOER^{normal}(-3.5ppm) - NOER^{tumor}(-3.5ppm)] \end{aligned} \quad [31]$$

Based on Eq. [30], the absolute APT-MRI signal intensity quantified by $\mathrm{MTR_{asym}}(3.5\mathrm{ppm})$ is reduced by the NOE effect. However, if the NOE is smaller in tumor than in contralateral brain tissue (an image contrast opposite to that of the APT effect), the APTw image contrast between tumor and contralateral brain tissue would increase due to the presence of the NOE. Thus, the NOE is actually a positive confounding factor in APTw image contrast in the tumor, based on an MTR asymmetry analysis.

# METHODS

## MRI Experiments

The MR imaging experiments were conducted on a horizontal bore Bruker 4.7 T Biospec animal imager, with a 7 cm inner diameter coil for RF transmission and a 2.5 cm surface coil for signal reception, which were actively decoupled. Six human glioblastoma-bearing adult Fisher 344 rats were scanned at 45 days post-implantation. First, high-resolution $T_2$-weighted images in the coronal plane were acquired with a fast spin echo sequence, using the following parameters: repetition time (TR) = 3000 ms; echo time (TE) = 64 ms; average of excitations (NEX) = 2; matrix size = 192 × 192; FOV = 32 × 32 $mm^2$; slice thickness = 1.5 mm; and five slices. Then, several quantitative MRI parameters were acquired, including $T_1$, $T_2$, isotropic apparent diffusion coefficient (ADC), and cerebral blood flow (CBF). The longitudinal relaxation time, $T_{1w}^{obs}$, was mapped using an inversion recovery spin-echo echo-planar imaging (EPI) sequence, with seven inversion recovery times = 0.05, 0.3, 0.6, 1.2, 1.8, 2.5, and 3.5 s; a pre-delay time = 3 s; TE = 30 ms; matrix size = 64 × 64; and NEX = 4. The transverse relaxation time, $T_{2w}^{obs}$, was mapped using a spin-echo EPI sequence, with seven TEs = 30, 40, 50, 60, 70, 80, and 90 ms; TR = 3 s; matrix size = 64 × 64; and NEX = 4. ADC maps were estimated using the conventional pulsed-gradient spin-echo diffusion sequence, with b-values = 0, 166.7, 333.3, 500, 666.7, 833.3, and 1000 s/$mm^2$; TR = 3 s; TE = 80 ms; matrix size = 64 × 64; and NEX = 8. CBF maps were collected using the arterial spin labeling technique (21), with TR = 6 s; TE = 30 ms; matrix size = 64 × 64; and NEX = 16. The label images were acquired at a distance of 20 mm away from the imaging slice.

CEST image data were obtained using a fat-suppressed spin-echo pulse sequence (consisting of a Gaussian-shaped, slice-selective excitation pulse of 1 ms and a Gaussian-shaped, chemical shift-selective refocusing pulse of 4 ms, together with gradient dephasing, as used in our previous studies (61)), with a long continuous-wave RF saturation pulse and a single-shot EPI readout (TR = 10 s; TE = 30 ms; matrix size = 64 × 64 $mm^2$; FOV = 32 × 32 $mm^2$; slice thickness = 1.5 mm; and RF saturation time = 4 s). Three sets of Z-spectra with 26 frequency offsets were acquired to quantify conventional MT, NOE, and APT effects, using three RF saturation powers (0.5, 1.3, and 2.1 μT) and NEX = 1: (1) $Z_{21\sim-21ppm}$: off ($S_0$ image for control), 21 to −21 ppm at intervals of 1.75 ppm for MT modeling with the super-Lorentzian lineshape; (2) $Z_{6\sim-6ppm}$: off, 6 to −6 ppm at intervals of 0.5 ppm for the quantification of NOE and APT effects; and (3) $Z_{1.2\sim-1.2ppm}$: off, 1.2 to −1.2 ppm at intervals of 0.1 ppm for water saturation shift referencing (WASSR)-based $B_0$ inhomogeneity corrections (62). In addition, high signal-to-noise ratio APT, using two frequency offsets (±3.5 ppm), and MTR(10ppm) images were acquired (NEX = 16), after the slab shimming (thickness 6 mm) and scanner transmitter frequency adjustment. The total scan time was about 90 min for each animal. Animal care throughout the experimental procedures in the study was in accordance with institutional guidelines.

## Data Processing and Fitting Procedure

All data processing was performed using Interactive Data Language (IDL, Version7; Exelis Visual Information Solutions, Inc., Boulder, CO) or MATLAB (The MathWorks, Inc., Natick, MA). Figure 1 shows the flow chart of the data processing procedures. First, the

WASSR method with $Z_{1.2\sim-1.2ppm}$ at 0.5 μT was used to correct for $B_0$ field inhomogeneity effects (62). All other Z-spectra ($Z_{21\sim-21ppm}$ and $Z_{6\sim-6ppm}$) at three power levels were interpolated and aligned correspondingly on a pixel-by-pixel basis along the direction of the offset axis. Then, the wide-offset data were fitted to Henkelman's two-pool MT model with the super-Lorentzian lineshape. Data points of small frequency offsets between 7 and −7 ppm in $B_0$-corrected $Z_{21\sim-21ppm}$ were excluded ($Z'_{21\sim-21ppm}$) to avoid APT and most NOE contributions prior to conventional MT modeling. The four independent MT model parameters ($R$, $T_{2m}$, $RM_0^mT_{1w}$, $T_{1w}/T_{2w}$) were obtained by fitting all modified $Z'_{21\sim-21ppm}$ data acquired from three different power $\omega_1$ values simultaneously to the two-pool MT model described in Eq. [3], based on the nonlinear least-squares fitting approach, which implemented the Levenberg-Marquardt algorithm. In this procedure, $M_0^w$ was conventionally normalized to 1. $T_{1m}$ was set as a constant value of 1 s because it could not well determined from fits (52, 56). The super-Lorentzian function, characterized by one parameter $T_{2m}$, was evaluated by the numerical integration. The quality of the estimated MT model parameters was evaluated by the root of the sum of the squared differences between the fitted and experimental data, and the $\chi^2$ goodness-of-fit metric. Finally, $Z_{EMR}$ in an offset range from 6 ~ −6 ppm was obtained, and $APT^{\#}$ and $NOE^{\#}$ were calculated.

In addition, a four-pool APT and NOE exchange model was also analytically solved with the *a priori* fitted two-pool MT information (obtained in combination with an independent MRI measurement of $T_{1w}^{obs}$), and the parameter fitting was performed using the minimum norm estimate. Our model fitting approach substantially reduced the risk of over-fitting and the uncertainties of direct four-pool model parameter estimates. In this study, this fitting procedure was based on regions of interest (ROIs).

$T_{1w}^{obs}$ was fitted using $I=A+Be^{-TI/T_{1w}^{obs}}$. $T_{2w}^{obs}$ was fitted using $I=I_0e^{-TE/T_{2w}^{obs}}$. The average ADC of water, $ADC_{av} = Trace(D)/3$, was fitted by $I = I_0e^{-b\cdot ADC_{av}}$. The CBF map was reconstructed from images with and without labeling (21). These quantitative MR parameters were fitted ( $T_{1w}^{obs}$, $T_{2w}^{obs}$, and ADC) or processed (CBF) on a pixel-by-pixel basis. To compare the MT, APT, and NOE parameters in the tumor, three ROIs enclosing the normal tissue, the tumor center, and the tumor rim were analyzed. These ROIs were carefully drawn on the ADC map. Tumor volumes were manually measured as the sum of all tumor voxels in all slices on the high-resolution $T_2$-weighted images. Data in graphs and tables are presented as mean ± SE. Statistical analysis was performed using a one-way ANOVA, followed by Tukey's post-hoc test. Statistical significance was considered at $p < 0.05$.

## RESULTS

Figure 2 shows the average two-pool MT fitted results from normal tissue, tissue in the tumor center, and tissue in the tumor rim (n = 6), with three RF saturation power levels. The super-Lorentzian lineshape was used to fit the semi-solid MT pool. The results show that the two-pool MT model accurately predicts the behavior of the semi-solid MT system for wide frequency offsets, yielding a close fit for the modified $Z'_{21\sim-21ppm}$ data, excluding 7 to −7 ppm. Table 1 summarizes the fitted ($R$, $T_{2m}$, $RM_0^mT_{1w}$, and $T_{1w}/T_{2w}$) and derived ($T_{1w}$, $T_{2w}$,

and $M_0^m$) MT model parameters. In addition, Supporting Table S1 compares the difference between these parameters fitted from $Z_{21\sim-21ppm}$ and $Z'_{21\sim-21ppm}$ data. Basically, these model parameters (except $T_{2m}$) were significantly different between the normal tissue and the tissue in the tumor center or rim ($p < 0.05$). Particularly, $M_0^m$ of the normal brain tissue was significantly higher than those of the tumor center and tumor rim ($p < 0.05$).

Figure 3 compares the measured $Z_{6\sim-6ppm}$ data, average four-pool fitted results using the $Z_{6\sim-6ppm}$ data, and EMR curves (namely, $Z_{EMR}$) fitted with the $Z'_{21\sim-21ppm}$ data from the contralateral normal brain, the tumor center, and the tumor rim for three RF saturation power levels. Supporting Fig. S1 further shows the simulated Z-spectra of the contralateral normal brain tissue, the tumor center, and the tumor rim with the two-pool semi-solid MT, three-pool, and four-pool models. The results show that the four-pool APT and NOE exchange model fitted the $Z_{6\sim-6ppm}$ behavior very well. Notably, the average $Z_{EMR}$ curves in three ROIs for all RF power levels overall showed higher signal intensities than the experimentally measured Z-spectra and the four-pool fitted curves for all frequency offsets close to water. The difference between the experimental Z-spectra and $Z_{EMR}$ curves clearly indicated the presence of the APT effects peaked at roughly 3.5 ppm downfield from water and the presence of the NOE effects primarily appeared at roughly −2.5 to −5 ppm upfield from water. The magnitude of these downfield APT and upfield NOE signals were dependent on RF saturation power and brain tissue type. Table 2 summarizes all four-pool fitted parameters for three ROIs. No significant differences were observed in both exchange rates and $T_2$ relaxation times of the APT- and NOE-related proton pools between the normal tissue, the tumor center, and the tumor rim. As expected, the APT-related pool sizes of the tumor center and the tumor rim were significantly larger than that of the normal tissue, while the NOE-related pool sizes of the tumor center and the tumor rim were significantly smaller than that of the normal tissue.

Figure 4a–c shows the quantitatively measured $APT^{\#}$ and $NOE^{\#}$ signal features as a function of frequency offsets obtained from the contralateral normal tissue, the tumor center, and the tumor rim at three RF saturation powers. Several important results can be observed. (i) The downfield $APT^{\#}$ signals of the tumor center and the tumor rim were both significantly higher than those of the normal tissue across all power levels ($p < 0.05$). (ii) The upfield $NOE^{\#}$ signals were generally lower in the tumor center and rim than in the normal tissue, which reached statistical significance ($p < 0.05$) in the tumor center at 1.3 μT. However, the $NOE^{\#}$ signals seemed higher in the tumor center than in the normal tissue at 0.5 μT, even though the difference was not statistically significant. (iii) The RF power dependencies of $APT^{\#}$ and $NOE^{\#}$ signals can be seen clearly. The $APT^{\#}$ signals were significantly smaller than the $NOE^{\#}$ signals at the lower RF power level in all ROIs (0.5 μT; $p < 0.05$), but became significantly larger than the $NOE^{\#}$ signals at the larger RF power levels for the tumor center and the tumor rim ( ≥1.3 μT; $p < 0.05$; except the normal tissue). The different power dependence of the $APT^{\#}$ and $NOE^{\#}$ peaks may be due to that fact that the amide proton exchange rate is faster than the NOE-related proton exchange rate (Table 2), resulting in a relatively higher optimal saturation power level for $APT^{\#}$ than for $NOE^{\#}$ (36). Figure 4d–f shows the corresponding simulated $APT^{\#}$ and $NOE^{\#}$ signal features obtained from the

contralateral normal tissue, the tumor center, and the tumor rim at three RF saturation powers, which were very similar to the results from the experimental data.

Figure 5 shows a comparison of the average Z-spectra and $MTR_{asym}$ spectra of the normal tissue, the tumor center, and the tumor rim at three RF saturation powers. As observed before (51), the $MTR_{asym}$(3.5ppm) values for all ROIs were negative at most frequency offsets due to larger upfield NOE effects at the lower RF power (0.5 μT). At the relatively higher RF saturation powers ( ≥1.3 μT), however, the downfield APT effects became more pronounced, and the $MTR_{asym}$(3.5ppm) increased and became positive for the tumor center and rim.

Figure 6 shows the image contrasts of $APT^{\#}$, $NOE^{\#}$, and $MTR_{asym}$(3.5ppm) between the tumor center or the rim and the contralateral normal brain tissue. It was found that (i) the downfield $APT^{\#}$ image contrasts between the tumor center or the rim and the contralateral normal tissue were all positive at the three RF saturation power levels ($p < 0.05$). (ii) Interestingly, the upfield $NOE^{\#}$ image contrasts between the tumor center or the rim and the contralateral normal tissue were negative at the three RF saturation power levels, except that between the tumor center and the contralateral normal tissue at 0.5 μT (which was positive). (iii) The absolute $APT^{\#}$ image contrasts between the tumor center or the rim and the contralateral normal tissue were consistently larger than corresponding absolute $NOE^{\#}$ contrasts at the three RF saturation powers ($p < 0.05$). (iv) The $MTR_{asym}$(3.5ppm) image contrasts between the tumor center or the rim and the contralateral normal tissue were all positive at the three RF saturation power levels ($p < 0.05$). Based on Eq. [31], these $MTR_{asym}$(3.5ppm) image contrasts were all dominated by the $APT^{\#}$ image contrasts. The calculated $MTR_{asym}$(3.5ppm) images are called APTw images (24).

Figure 7 shows quantitative multi-parametric MRI maps of a representative tumor-bearing rat. Tumor volumes for all six rats were roughly estimated to be 111.4 ± 48.4 $mm^3$. It can be seen that the tumor was hyperintense on $T_1$, $T_2$, and ADC maps and hypointense on blood flow and MTR(10ppm) maps, compared to the contralateral normal brain tissue. Notably, the tumor was hyperintense on $MTR_{asym}$(3.5ppm) images and $APT^{\#}$ maps, but seemingly hypointense on $NOE^{\#}$ maps. Consistent with Fig. 4, the $APT^{\#}$ signals in all regions were lowest at the RF saturation power of 0.5 μT and seemingly peaked at 1.3 μT, while the $NOE^{\#}$ signals were lowest at 2.1 μT. Consistent with Fig. 5, the $MTR_{asym}$(3.5ppm) signals in all ROIs were highest at the 2.1 μT.

## DISCUSSION

In this study, we have introduced a novel EMR approach based on Henkelman's two-pool MT model with a super-Lorentzian lineshape to quantify APT and NOE signals ($APT^{\#}$ and $NOE^{\#}$). It is well known that the two-pool system, combined with the super-Lorentzian RF absorption lineshape for semi-solid protons, can describe the behavior of the conventional MT signal as a function of RF saturation frequency and amplitude with a good quality of fit. We fitted the model parameters ($R$, $T_{2m}$, $RM_0^m T_{1w}$, $T_{1w}/T_{2w}$) with the wide-offset experimental data, namely, $Z'_{21\sim-21ppm}$, excluding the data points of small frequency offsets between 7 and −7 ppm. Thus, APT and most NOE contributions should be minimized in our

MT modeling, and the obtained $Z_{EMR}$ curves in an offset range (6 ~ −6 ppm) should include only DS and semi-solid MT effects. Thus, the EMR approach has the potential to be an important and accurate CEST-MRI quantitative technique. Based on Fig. 3, on the contrary, when the average of two boundary images acquired at 3 and 4 ppm was used as the reference image for APT*, and the average acquired at −2 and −5 ppm was used as the reference image for NOE* (the three-offset method (36)), the obtained APT* and NOE* would be underestimated in all cases.

According to Eq. [30] and Fig. 5d–f, the APTw image signal quantified by $MTR_{asym}(3.5ppm)$ was reduced by the NOE effect, and even became negative. However, because the NOE effect had an image contrast opposite to the APT effect in the whole tumor (center and rim), the APTw image contrast between the tumor center and rim and contralateral brain tissue increased due to the presence of the NOE (Eq. [31], Fig. 6). Thus, the NOE was actually a positive confounding factor in APTw image contrast in the tumor, based on an MTR asymmetry analysis. This study has clearly shown that $MTR_{asym}(3.5ppm)$ is a useful and reliable metric for APT-MRI. Indeed, several recent human studies have shown that the APTw imaging signal quantified by $MTR_{asym}(3.5ppm)$ is a powerful clinical indicator of cancers (24–29) and strokes (22, 23).

Consistent with our two-pool MT fitted results (Table 1), Quesson et al. previously observed that the fitted value significantly increased, and the $RM_0^m T_{1w}$, $T_{1w}/T_{2w}$, and $M_0^m$ values significantly decreased in C6 tumor, compared to normal tissue (63). Our fitted parameters had relatively low values, presumably due to differences in the sequence parameters and the tumor model. Further, the fitted amide proton exchange rates by the four-pool APT and NOE model (Table 2) were consistent with the previous MRS study (16), and, as expected, showed no significant difference between the tumor and normal tissue. Notably, as expected, the semi-solid MT pool sizes of the tumor center and rim were significantly smaller than that of the normal tissue (Table 1), while the mobile APT pool sizes of the tumor center and rim were significantly larger than that of the normal tissue (Table 2), consistent with the MTR(10ppm) and APT# measurements (Fig. 7). It was reported recently (64) that, after corrections for spillover, MT, and $T_{1w}$ effects, the corrected APT signal in 9L tumor was not significantly different from that in normal brain tissue ($AREX_{tumor} \approx AREX_{normal}$), consistent with the biochemical measurements. However, the total protein (mobile and semi-solid) contents measured by the Bradford and bicinchoninic acid assay (BCA) methods should not be used to elucidate APT contrast mechanisms in biological tissues which, in principle, result from mobile proteins and peptides only. Indeed, the water content is usually higher, and $T_{1w}$ is enhanced in tumor. However, it is extremely important to understand that these two changes are mostly compensated for in many diseases in the APT measurements (16). Therefore, assessing the influence of the water longitudinal relaxation *in vivo* on APT (and also NOE) imaging should be performed cautiously, and simply multiplying by $R_{1w}$ would lead to an erroneous result (64).

Finally, we would like to point out several potential issues in this study. (i) Since the conventional semi-solid MT effect is assumed symmetric around the water resonance, and both mobile and asymmetric, relatively less mobile biomolecules are combined into a single NOE-related pool, the obtained NOE# signals would be larger. (ii) Many previous studies

have demonstrated that side-chain amine protons of mobile proteins and peptides (~2 ppm) (6, 65, 66), amine protons in glutamate (~3 ppm) (9), and other NOE-related protons (about −1.6 ppm) (67) may make contributions to downfield CEST and upfield NOE signals. Thus, our measured results for the $APT^{\#}$ and $NOE^{\#}$ would be overestimated. Future studies are needed to fully isolate these sources by modeling systems with even more pools. (iii) A four-pool model consisting of semi-solid protons, amide protons (3.5 ppm downfield from water), and NOE-related protons (−3.5 ppm upfield from water) was used to quantify APT and NOE effects in this study. In Supporting Fig. S2, we compared seven pools [water, semi-solid, amide, amine, hydroxyl, NOE-related at −3.5 ppm (including mobile protons and asymmetric, relatively less mobile protons), and NOE-related at −1.6 ppm] and four pools [water, semi-solid, amide, NOE-related at −3.5 ppm (including mobile protons and asymmetric, relatively less mobile protons)]. Our result shows that there are only small differences in simulated APT and NOE signals between seven-pool and four-pool fitting. Therefore, the four-pool fitting (with the benefits of much fewer free parameters) could still give very good APT and NOE results, even though even more pools may definitely be useful for the quantification of other CEST signals.

## CONCLUSIONS

To quantitatively assess APT and NOE effects *in vivo*, a new and straightforward fitting approach (EMR) has been introduced, which is based on the extrapolated semi-solid MT model reference signals. In the initial application, we quantitatively investigated MT, APT, and NOE signal features in a rat brain tumor model at 4.7 T. The quantitative results showed that the $APT^{\#}$ signals were significantly higher in the tumor center or in the rim than in the normal tissue at all saturation powers, and were the major contributor to the APTw (namely, $MTR_{asym}(3.5ppm)$) image contrast in the tumor compared to the normal brain tissue. The NOE effect is a positive confounding factor for the APTw image contrast, and the NOE contrast would be added to APTw. The EMR-based four-pool fitting showed that there were no significant differences between the exchange rates of the APT- and NOE-related proton pools in the normal tissue, the tumor center, and the tumor rim. The amide proton pool sizes of the tumor center and rim were significantly larger than that of the normal tissue, while the NOE-related pool sizes of the tumor center and rim were significantly smaller than that of the normal tissue. The EMR approach is straightforward and more accurate for quantitatively measuring pure APT, NOE, and other CEST signals. The quantitative results would provide some insight into the mechanisms of APT and NOE effects in tissue, help to establish a ratio-metric for pH measurements (for example, using the CEST signals at 3.5 and 2 ppm), as well as help to optimize CEST imaging parameters and protocols.

## Supplementary Material

Refer to Web version on PubMed Central for supplementary material.

## Acknowledgments

The authors thank Drs. Bo Ma and Bachchu Lal for experimental assistance, and Ms. Mary McAllister for editorial assistance. This work was supported in part by grants from the National Institutes of Health (R01EB009731, R01CA166171, R01NS083435, and R21EB015555).

## References


1. Ward KM, Aletras AH, Balaban RS. A new class of contrast agents for MRI based on proton chemical exchange dependent saturation transfer (CEST). J Magn Reson. 2000; 143:79–87. [PubMed: 10698648]
2. Zhou J, van Zijl PC. Chemical exchange saturation transfer imaging and spectroscopy. Progr NMR Spectr. 2006; 48:109–136.
3. Sherry AD, Woods M. Chemical exchange saturation transfer contrast agents for magnetic resonance imaging. Annu Rev Biomed Eng. 2008; 10:391–411. [PubMed: 18647117]
4. van Zijl PCM, Yadav NN. Chemical exchange saturation transfer (CEST): What is in a name and what isn't? Magn Reson Med. 2011; 65:927–948. [PubMed: 21337419]
5. Vinogradov E, Sherry AD, Lenkinski RE. CEST: From basic principles to applications, challenges and opportunities. J Magn Reson. 2013; 229:155–172. [PubMed: 23273841]
6. Zhou J, Lal B, Wilson DA, Laterra J, van Zijl PCM. Amide proton transfer (APT) contrast for imaging of brain tumors. Magn Reson Med. 2003; 50:1120–1126. [PubMed: 14648559]
7. Jones CK, Schlosser MJ, van Zijl PC, Pomper MG, Golay X, Zhou J. Amide proton transfer imaging of human brain tumors at 3T. Magn Reson Med. 2006; 56:585–592. [PubMed: 16892186]
8. Ling W, Regatte RR, Navon G, Jerschow A. Assessment of glycosaminoglycan concentration in vivo by chemical exchange-dependent saturation transfer (gagCEST). Proc Natl Acad Sci (USA). 2008; 105:2266–2270. [PubMed: 18268341]
9. Cai KJ, Haris M, Singh A, Kogan F, Greenberg JH, Hariharan H, Detre JA, Reddy R. Magnetic resonance imaging of glutamate. Nature Med. 2012; 18:302–306. [PubMed: 22270722]
10. Haris M, Singh A, Cai K, Kogan F, McGarvey J, Debrosse C, Zsido GA, Witschey WR, Koomalsingh K, Pilla JJ, Chirinos JA, Ferrari VA, Gorman JH, Hariharan H, Gorman RC, Reddy R. A technique for in vivo mapping of myocardial creatine kinase metabolism. Nature Med. 2014; 20:209–214. [PubMed: 24412924]
11. Chan KWY, McMahon MT, Kato Y, Liu GS, Bulte JWM, Bhujwalla ZM, Artemov D, van Zijl PCM. Natural D-glucose as a biodegradable MRI contrast agent for detecting cancer. Magn Reson Med. 2012; 68:1764–1773. [PubMed: 23074027]
12. Walker-Samuel S, Ramasawmy R, Torrealdea F, Rega M, Rajkumar V, Johnson SP, Richardson S, Gonçalves M, Parkes HG, Årstad E, Thomas D, Pedley RB, Lythgoe MF, Golay X. In vivo imaging of glucose uptake and metabolism in tumors. Nature Med. 2013; 19:1067–1072. [PubMed: 23832090]
13. Zhang S, Winter P, Wu K, Sherry AD. A novel europium(III)-based MRI contrast agent. J Am Chem Soc. 2001; 123:1517–1578. [PubMed: 11456734]
14. Aime S, Calabi L, Biondi L, De Miranda M, Ghelli S, Paleari L, Rebaudengo C, Terreno E. Iopamidol: Exploring the potential use of a well-established X-ray contrast agent for MRI. Magn Reson Med. 2005; 53:830–834. [PubMed: 15799043]
15. Liu GS, Li YG, Pagel MD. Design and characterization of a new irreversible responsive PARACEST MRI contrast agent that detects nitric oxide. Magn Reson Med. 2007; 58:1249–1256. [PubMed: 18046705]
16. Zhou J, Payen J, Wilson DA, Traystman RJ, van Zijl PCM. Using the amide proton signals of intracellular proteins and peptides to detect pH effects in MRI. Nature Med. 2003; 9:1085–1090. [PubMed: 12872167]
17. Zhang SR, Malloy CR, Sherry AD. MRI thermometry based on PARACEST agents. J Am Chem Soc. 2005; 127:17572–17573. [PubMed: 16351064]
18. Zhou J, Wilson DA, Sun PZ, Klaus JA, van Zijl PCM. Quantitative description of proton exchange processes between water and endogenous and exogenous agents for WEX, CEST, and APT experiments. Magn Reson Med. 2004; 51:945–952. [PubMed: 15122676]
19. Englander SW, Downer NW, Teitelbaum H. Hydrogen exchange. Annu Rev Biochem. 1972; 41:903–924. [PubMed: 4563445]
20. Zhou JY, van Zijl PCM. Defining an acidosis-based ischemic penumbra from pH-weighted MRI. Transl Stroke Res. 2012; 3:76–83. [PubMed: 22408691]

21. Sun PZ, Zhou J, Sun W, Huang J, van Zijl PCM. Detection of the ischemic penumbra using pH-weighted MRI. J Cereb Blood Flow Metab. 2007; 27:1129–1136. [PubMed: 17133226]
22. Tietze A, Blicher J, Mikkelsen IK, Ostergaard L, Strother MK, Smith SA, Donahue MJ. Assessment of ischemic penumbra in patients with hyperacute stroke using amide proton transfer (APT) chemical exchange saturation transfer (CEST) MRI. NMR Biomed. 2014; 27:163–174. [PubMed: 24288260]
23. Tee YK, Harston GW, Blockley N, Okell TW, Levman J, Sheerin F, Cellerini M, Jezzard P, Kennedy J, Payne SJ, Chappell MA. Comparing different analysis methods for quantifying the MRI amide proton transfer (APT) effect in hyperacute stroke patients. NMR Biomed. 201410.1002/nbm.3147
24. Zhou J, Blakeley JO, Hua J, Kim M, Laterra J, Pomper MG, van Zijl PCM. Practical data acquisition method for human brain tumor amide proton transfer (APT) imaging. Magn Reson Med. 2008; 60:842–849. [PubMed: 18816868]
25. Wen Z, Hu S, Huang F, Wang X, Guo L, Quan X, Wang S, Zhou J. MR imaging of high-grade brain tumors using endogenous protein and peptide-based contrast. NeuroImage. 2010; 51:616–622. [PubMed: 20188197]
26. Zhou J, Zhu H, Lim M, Blair L, Quinones-Hinojosa A, Messina AA, Eberhart CG, Pomper MG, Laterra J, Barker PB, van Zijl PCM, Blakeley JO. Three-dimensional amide proton transfer MR imaging of gliomas: Initial experience and comparison with gadolinium enhancement. J Magn Reson Imaging. 2013; 38:1119–1128. [PubMed: 23440878]
27. Togao O, Yoshiura T, Keupp J, Hiwatashi A, Yamashita K, Kikuchi K, Suzuki Y, Suzuki SO, Iwaki T, Hata N, Mizoguchi M, Yoshimoto K, Sagiyama K, Takahashi M, Honda H. Amide proton transfer imaging of adult diffuse gliomas: correlation with histopathological grades. Neuro Oncol. 2014; 16:441–448. [PubMed: 24305718]
28. Jia G, Abaza R, Williams JD, Zynger DL, Zhou JY, Shah ZK, Patel M, Sammet S, Wei L, Bahnson RR, Knopp MV. Amide proton transfer MR imaging of prostate cancer: A preliminary study. J Magn Reson Imaging. 2011; 33:647–654. [PubMed: 21563248]
29. Dula AN, Arlinghaus LR, Dortch RD, Dewey BE, Whisenant JG, Ayers GD, Yankeelov TE, Smith SA. Amide proton transfer imaging of the breast at 3 T: Establishing reproducibility and possible feasibility assessing chemotherapy response. Magn Reson Med. 2013; 70:216–224. [PubMed: 22907893]
30. Togao O, Kessinger CW, Huang G, Soesbe TC, Sagiyama K, Dimitrov I, Sherry AD, Gao J, Takahashi M. Characterization of lung cancer by amide proton transfer (APT) imaging: an in-vivo study in an orthotopic mouse model. PLoS One. 2013; 8:e77019. [PubMed: 24143199]
31. Zhou J, Tryggestad E, Wen Z, Lal B, Zhou T, Grossman R, Wang S, Yan K, Fu D-X, Ford E, Tyler B, Blakeley J, Laterra J, van Zijl PCM. Differentiation between glioma and radiation necrosis using molecular magnetic resonance imaging of endogenous proteins and peptides. Nature Med. 2011; 17:130–134. [PubMed: 21170048]
32. Hong X, Liu L, Wang M, Ding K, Fan Y, Ma B, Lal B, Tyler B, Mangraviti A, Wang S, Wong J, Laterra J, Zhou J. Quantitative multiparametric MRI assessment of glioma response to radiotherapy in a rat model. Neuro Oncol. 2014; 16:856–867. [PubMed: 24366911]
33. Sagiyama K, Mashimo T, Togao O, Vemireddy V, Hatanpaa KJ, Maher EA, Mickey BE, Pan E, Sherry AD, Bachoo RM, Takahashi M. In vivo chemical exchange saturation transfer imaging allows early detection of a therapeutic response in glioblastoma. Proc Natl Acad Sci (USA). 2014; 111:4542–4547. [PubMed: 24616497]
34. Zhao X, Wen Z, Huang F, Lu S, Wang X, Hu S, Zu D, Zhou J. Saturation power dependence of amide proton transfer image contrasts in human brain tumors and strokes at 3 T. Magn Reson Med. 2011; 66:1033–1041. [PubMed: 21394783]
35. Jones CK, Huang A, Xu J, Edden RA, Schar M, Hua J, Oskolkov N, Zaca D, Zhou J, McMahon MT, Pillai JJ, van Zijl PC. Nuclear Overhauser enhancement (NOE) imaging in the human brain at 7T. Neuroimage. 2013; 77:114–124. [PubMed: 23567889]
36. Jin T, Wang P, Zong X, Kim S-G. MR imaging of the amide-proton transfer effect and the pH-insensitive nuclear overhauser effect at 9. 4 T. Magn Reson Med. 2013; 69:760–770. [PubMed: 22577042]

37. Liu D, Zhou J, Xue R, Zuo Z, An J, Wang DJJ. Quantitative characterization of nuclear Overhauser enhancement and amide proton transfer effects in the human brain at 7 Tesla. Magn Reson Med. 2013; 70:1070–1081. [PubMed: 23238951]
38. Mougin O, Clemence M, Peters A, Pitiot A, Gowland P. High-resolution imaging of magnetisation transfer and nuclear Overhauser effect in the human visual cortex at 7 T. NMR Biomed. 2013; 26:1508–1517. [PubMed: 23801569]
39. Desmond KL, Moosvi F, Stanisz GJ. Mapping of amide, amine, and aliphatic peaks in the CEST spectra of murine xenografts at 7 T. Magn Reson Med. 2014; 71:1841–1853. [PubMed: 23801344]
40. Lu J, Zhou J, Cai C, Cai S, Chen Z. Observation of true and pseudo NOE signals using CEST-MRI and CEST-MRS sequences with and without lipid suppression. Magn Reson Med. 201410.1002/mrm.25277
41. Liepinsh E, Otting G. Proton exchange rates from amino acid side chains-implication for image contrast. Magn Reson Med. 1996; 35:30–42. [PubMed: 8771020]
42. van Zijl PCM, Zhou J, Mori N, Payen J, Mori S. Mechanism of magnetization transfer during on-resonance water saturation. A new approach to detect mobile proteins, peptides, and lipids. Magn Reson Med. 2003; 49:440–449. [PubMed: 12594746]
43. Zaiss M, Schmitt B, Bachert P. Quantitative separation of CEST effect from magnetization transfer and spillover effects by Lorentzian-line-fit analysis of z-spectra. J Magn Reson. 2011; 211:149–155. [PubMed: 21641247]
44. Jones CK, Polders D, Hua J, Zhe H, Hoogduin HJ, Zhou J, Luijten P, van Zijl PCM. In vivo 3D whole-brain pulsed steady state chemical exchange saturation transfer at 7T. Magn Reson Med. 2012; 67:1579–1589. [PubMed: 22083645]
45. Chappell MA, Donahue MJ, Tee YK, Khrapitchev AA, Sibson NR, Jezzard P, Payne SJ. Quantitative Bayesian model-based analysis of amide proton transfer MRI. Magn Reson Med. 2013; 70:556–567. [PubMed: 23008121]
46. McVicar N, Li AX, Goncalves DF, Bellyou M, Meakin SO, Prado MA, Bartha R. Quantitative tissue pH measurement during cerebral ischemia using amine and amide concentration-independent detection (AACID) with MRI. J Cereb Blood Flow Metab. 2014; 34:690–698. [PubMed: 24496171]
47. Lee JS, Regatte RR, Jerschow A. Isolating chemical exchange saturation transfer contrast from magnetization transfer asymmetry under two-frequency rf irradiation. J Magn Reson. 2012; 215:56–63. [PubMed: 22237631]
48. Zu ZL, Janve VA, Li K, Does MD, Gore JC, Gochberg DF. Multi-angle ratiometric approach to measure chemical exchange in amide proton transfer imaging. Magn Reson Med. 2012; 68:711–719. [PubMed: 22161770]
49. Swanson, SD.; Pang, Y. MT is symmetric but shifted with respect to water. Proc 11th Annual Meeting ISMRM; Toronto. 2003. p. 660
50. Hua J, Jones CK, Blakeley J, Smith SA, van Zijl PCM, Zhou J. Quantitative description of the asymmetry in magnetization transfer effects around the water resonance in the human brain. Magn Reson Med. 2007; 58:786–793. [PubMed: 17899597]
51. Zhou J, Hong X, Zhao X, Gao J-H, Yuan J. APT-weighted and NOE-weighted image contrasts in glioma with different RF saturation powers based on magnetization transfer ratio asymmetry analyses. Magn Reson Med. 2013; 70:320–327. [PubMed: 23661598]
52. Henkelman RM, Huang X, Xiang Q-S, Stanisz GJ, Swanson SD, Bronskill MJ. Quantitative interpretation of magnetization transfer. Magn Reson Med. 1993; 29:759–766. [PubMed: 8350718]
53. Stanisz GJ, Kecojevic A, Bronskill MJ, Henkelman RM. Characterizing white matter with magnetization transfer and T(2). Magn Reson Med. 1999; 42:1128–1136. [PubMed: 10571935]
54. Morrison C, Henkelman RM. A model for magnetization transfer in tissues. Magn Reson Med. 1995; 33:475–482. [PubMed: 7776877]
55. Sled JG, Pike GB. Quantitative imaging of magnetization transfer exchange and relaxation properties in vivo using MRI. Magn Reson Med. 2001; 46:923–931. [PubMed: 11675644]

56. Ramani A, Dalton C, Miller DH, Tofts PS, Barker GJ. Precise estimate of fundamental in-vivo MT parameters in human brain in clinically feasible times. Magn Reson Imaging. 2002; 20:721–731. [PubMed: 12591568]
57. Woessner DE, Zhang S, Merritt ME, Sherry AD. Numerical solution of the Bloch equations provides insights into the optimum design of PARACEST agents for MRI. Magn Reson Med. 2005; 53:790–799. [PubMed: 15799055]
58. Li AX, Hudson RH, Barrett JW, Jones CK, Pasternak SH, Bartha R. Four-pool modeling of proton exchange processes in biological systems in the presence of MRI-paramagnetic chemical exchange saturation transfer (PARACEST) agents. Magn Reson Med. 2008; 60:1197–1206. [PubMed: 18958857]
59. Sun PZ. Simplified and scalable numerical solution for describing multi-pool chemical exchange saturation transfer (CEST) MRI contrast. J Magn Reson. 2010; 205:235–241. [PubMed: 20570196]
60. Zaiss M, Bachert P. Chemical exchange saturation transfer (CEST) and MR Z-spectroscopy in vivo: a review of theoretical approaches and methods. Phys Med Biol. 2013; 58:R221–R269. [PubMed: 24201125]
61. Sun PZ, Zhou J, Sun W, Huang J, van Zijl PC. Suppression of lipid artifacts in amide proton transfer (APT) imaging. Magn Reson Med. 2005; 54:222–225. [PubMed: 15968669]
62. Kim M, Gillen J, Landman BA, Zhou J, van Zijl PCM. Water saturation shift referencing (WASSR) for chemical exchange saturation transfer (CEST) experiments. Magn Reson Med. 2009; 61:1441–1450. [PubMed: 19358232]
63. Quesson B, Bouzier AK, Thiaudiere E, Delalande C, Merle M, Canioni P. Magnetization transfer fast imaging of implanted glioma in the rat brain at 4. 7 T: interpretation using a binary spin-bath model. J Magn Reson Imaging. 1997; 7:1076–1083. [PubMed: 9400852]
64. Xu J, Zaiss M, Zu Z, Li H, Xie J, Gochberg DF, Bachert P, Gore JC. On the origins of chemical exchange saturation transfer (CEST) contrast in tumors at 9. 4 T. NMR Biomed. 2014; 27:406–416. [PubMed: 24474497]
65. Salhotra A, Lal B, Laterra J, Sun PZ, van Zijl PCM, Zhou J. Amide proton transfer imaging of 9L gliosarcoma and human glioblastoma xenografts. NMR Biomed. 2008; 21:489–497. [PubMed: 17924591]
66. Jin T, Wang P, Zong XP, Kim SG. Magnetic resonance imaging of the Amine-Proton EXchange (APEX) dependent contrast. NeuroImage. 2012; 59:1218–1227. [PubMed: 21871570]
67. Zu Z, Xu J, Li H, Chekmenev EY, Quarles CC, Does MD, Gore JC, Gochberg DF. Imaging amide proton transfer and nuclear overhauser enhancement using chemical exchange rotation transfer (CERT). Magn Reson Med. 2014; 72:471–476. [PubMed: 24302497]

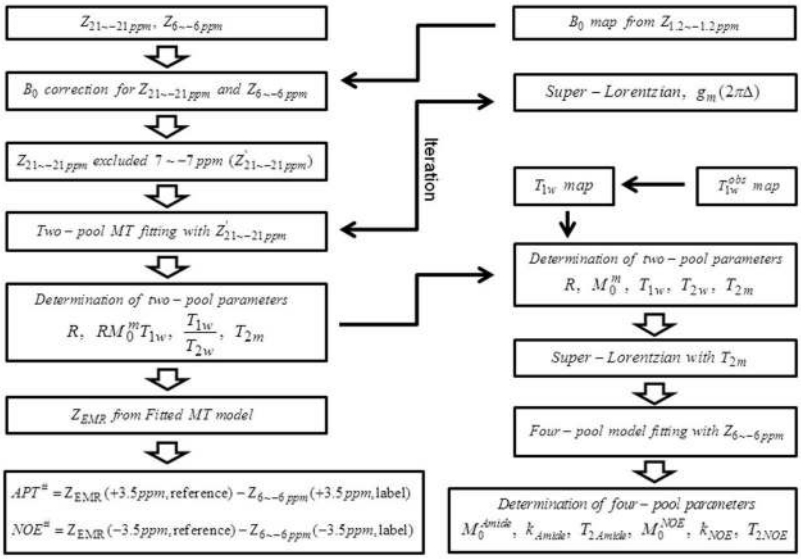


**Figure 1.**

Flow chart of data processing procedures for APT# and NOE#. After $B_0$ corrections with WASSR, the wide-offset $Z'_{21\sim-21ppm}$ was fitted to the two-pool MT model with a super-Lorentzian lineshape, and $R$, $T_{2m}$, $RM_0^m T_{1w}$, and $T_{1w}/T_{2w}$ were determined from the MT fitting routine. The fitting could be either ROI-based or pixel-based. Based on $T_{1w}^{obs}$ measured from an independent inversion recovery experiment, $T_{1w}$ could be calculated. This information allowed for the calculation of all physical parameters of the two-pool MT model. By subtracting experimental data ($Z_{6\sim-6ppm}$) or simulated four-pool data from $Z_{EMR}$ from the two-pool MT model, APT# and NOE# signals could be obtained. A four-pool APT and NOE exchange model can be analytically solved with the fitted MT information.

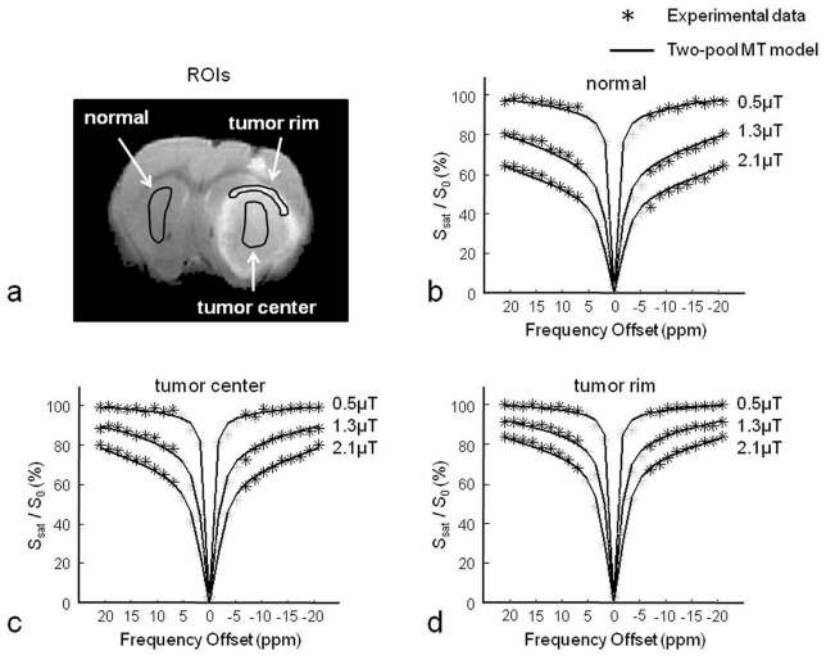


**Figure 2.**

Average two-pool MT fitted results (solid line) and experimental data (black asterisk) obtained from the contralateral normal tissue, the tumor center, and the tumor rim at three RF saturation powers (n = 6). The two-pool conventional MT model consisted of bulk water protons and semi-solid macromolecular protons. For the accurate semi-solid MT fit, $Z_{21\sim-21ppm}$ data for frequency offsets between 7 and −7 ppm were excluded to remove CEST and most NOE effects close to the water resonance. **a**: Example of ROIs. **b–d**: Results for the contralateral normal brain tissue, the tumor center, and the tumor rim, respectively.

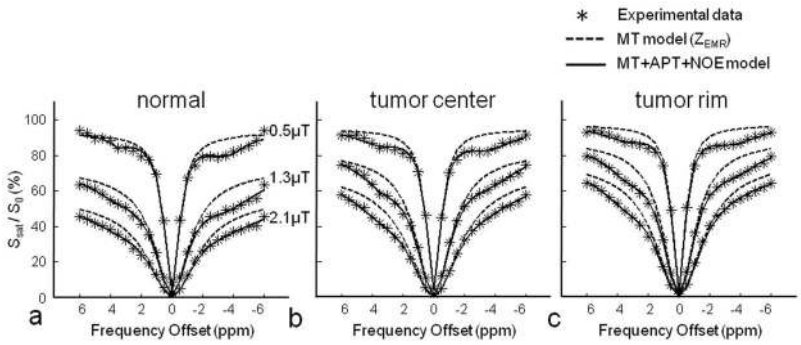


**Figure 3.**

Average ROI-based four-pool fitted results (solid line), experimental data (black asterisk), and extrapolated two-pool MT fitted curves ($Z_{EMR}$, dashed line) from the contralateral normal tissue (**a**), the tumor center (**b**), and the tumor rim (**c**) at three RF saturation powers (n = 6). The four-pool APT and NOE model consisted of bulk water protons, semi-solid macromolecular protons, amide protons, and NOE-related protons. These experimental and simulated Z-spectrum features clearly indicated the APT effects peaked at roughly 3.5 ppm from water, and the NOE effects primarily appeared at roughly −2.5 to −5 ppm from water.

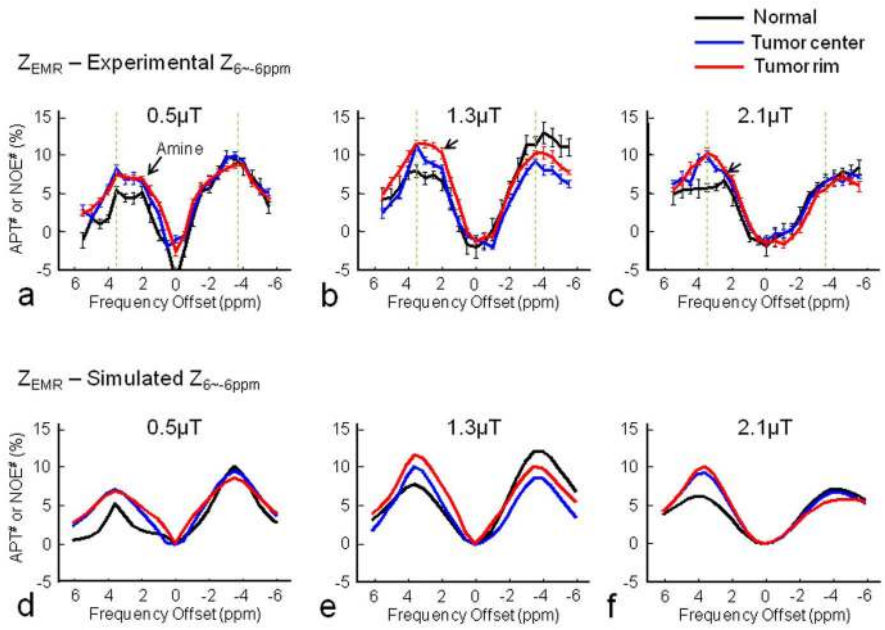


**Figure 4.**

Experimental (**a–c**) and simulated (**d–f**) downfield APT$^{\#}$ and upfield NOE$^{\#}$ signal features obtained from the contralateral normal tissue (black), the tumor center (blue), and the tumor rim (red) at three RF saturation power levels of 0.5, 1.3, and 2.1 μT. Experimental results (a–c) were obtained by subtracting the experimental measured Z-spectra (asterisks as shown in Fig 3) from the $Z_{EMR}$ data (dashed lines as shown in Fig 3). Error bars depict standard errors. The APT effects peaked at roughly 3.5 ppm downfield from water, and the NOE effects primarily appeared at roughly −2.5 to −5 ppm upfield from water. Simulated results (d–f) were obtained by subtracting the four-pool simulated Z-spectra (solid lines as shown in Fig 3) from the $Z_{EMR}$ data (dashed lines as shown in Fig 3).

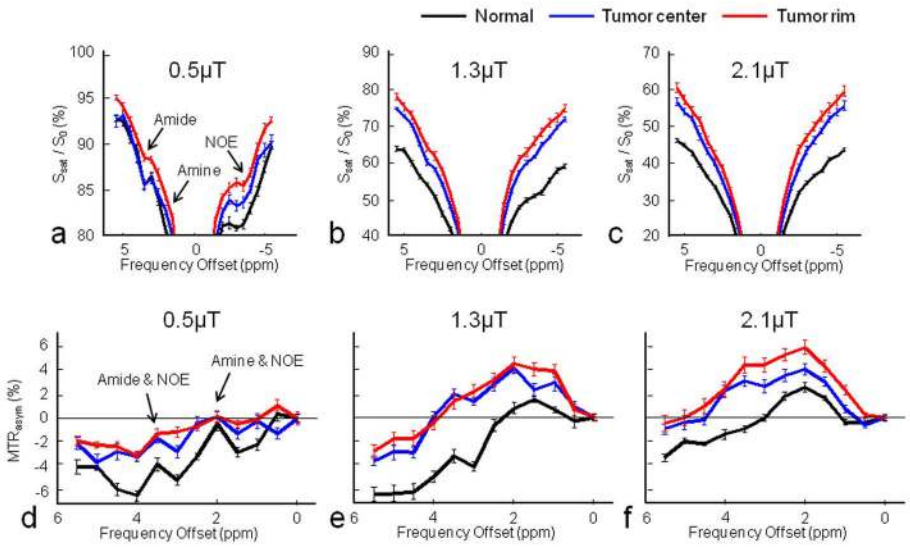


**Figure 5.**

Average Z-spectra (**a–c**) and $MTR_{asym}$ spectra (**d–f**) of the normal tissue (black), the tumor center (blue), and the tumor rim (red) from six rats at three RF saturation powers. Large upfield NOE signals caused large negative $MTR_{asym}$(3.5ppm) values in all ROIs at the lower RF power (0.5 μT) and in the normal brain tissue at the larger RF power levels ( ≥1.3 μT).

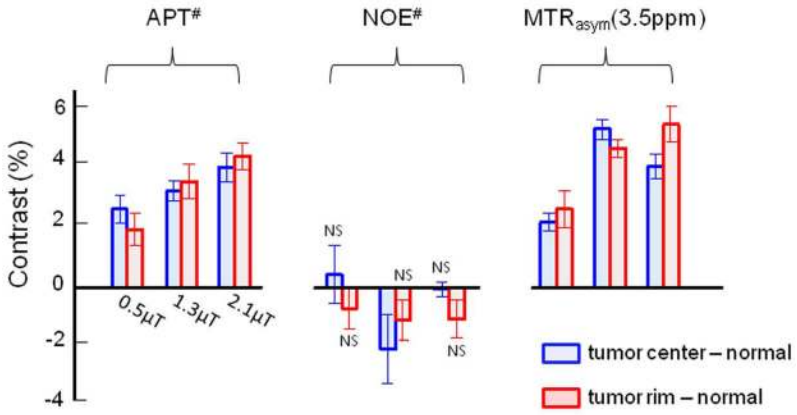


**Figure 6.**

Average APT$^{\#}$, NOE$^{\#}$, and MTR$_{asym}$(3.5ppm) image contrasts between the normal tissue and the tumor center or the rim (values at the tumor center or the rim – values at normal tissue). Error bars depict standard errors. All values are statistically significant ($p < 0.05$) unless otherwise indicated. NS indicates not statistically significant. As described by Eq. [31], MTR$_{asym}$(3.5ppm) image contrasts are mostly attributable to the APT$^{\#}$ contribution.

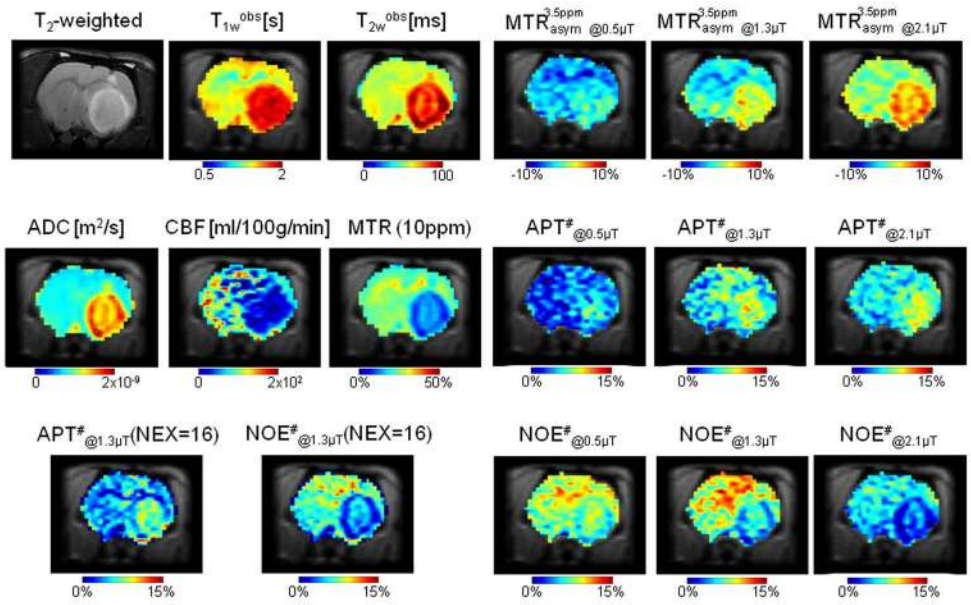


**Figure 7.**

Quantitative MR multi-parametric maps overlaid on a corresponding $T_2$-weighted image for a representative tumor-bearing rat (45 days post-tumor implantation).

**Table 1**

Fitted two-pool MT model parameters for the contralateral normal brain tissue, the tumor center, and the tumor rim (mean ± standard error)

| *n=6* | $R(s^{-1})$ | $T_{2m}(\mu s)$ | $RM_0^mT_{1w}$ | $T_{1w}/T_{2w}$ | $T_{2w}(ms)$ | $T_{1w}(s)$ | $T_{1w}^{obs}(s)$ | $M_0^m(\%)$ | $\chi^2$ |
|---|---|---|---|---|---|---|---|---|---|
| *Normal (N)* | 17.7 ± 0.8 | 18.7 ± 1.6 | 2.17 ± 0.15 | 44.6 ± 0.5 | 31.5 ± 0.4 | 1.40 ± 0.02 | 1.36 ± 0.02 | 8.7 ± 0.7 | $7.2\times10^{-4}$ |
| *Tumor center (TC)* | 20.3 ± 1.3 | 19.8 ± 0.4 | 1.39 ± 0.14 | 39.4 ± 0.9 | 50.0 ± 0.9 | 1.97 ± 0.05 | 1.91 ± 0.05 | 3.6 ± 0.3 | $7.5\times10^{-4}$ |
| *Tumor rim (TR)* | 21.5 ± 1.1 | 18.5 ± 1.2 | 1.34 ± 0.04 | 29.9 ± 0.5 | 64.7 ± 0.8 | 1.93 ± 0.04 | 1.88 ± 0.05 | 3.1 ± 0.2 | $9.2\times10^{-4}$ |
| *Post-hoc* | *N<TC,TR* | | *N>TC,TR* | *N>TC>TR* | *N<TC<TR* | *N<TC,TR* | *N<TC,TR* | *N>TC>TR* | |

$M_0^w$ was conventionally normalized to 1. $T_{1m}$ was set as a constant value of 1 s. The post-hoc test was performed for $p < 0.05$. <: significantly smaller; >: significantly larger; not indicated: no significant difference.

**Table 2**

Fitted four-pool proton exchange model parameters for the contralateral normal brain tissue, the tumor center, and the tumor rim (mean ± standard error)

| | *Amide proton pool* | | | *NOE-related proton pool* | | | |
|---|---|---|---|---|---|---|---|
| ***n = 6*** | $M_0^{s_1}(\%)$ | $k_{s_1w}(Hz)$ | $T_{2s_1}(ms)$ | $M_0^{s_2}(\%)$ | $k_{s_2w}(Hz)$ | $T_{2s_2}(ms)$ | $\chi^2$ |
| *Normal (N)* | 0.31 ± 0.03 | 23.9 ± 6.8 | 11.5 ± 1.1 | 0.66 ± 0.22 | 16.3 ± 8.3 | 0.40 ± 0.1 | $6.8\times10^{-4}$ |
| *Tumor center (TC)* | 0.39 ± 0.03 | 21.5 ± 2.5 | 10.1 ± 3.4 | 0.39 ± 0.07 | 17.6 ± 4.1 | 0.38 ± 0.2 | $6.1\times10^{-4}$ |
| *Tumor rim (TR)* | 0.40 ± 0.05 | 28.3 ± 9.6 | 11.2 ± 2.5 | 0.36 ± 0.13 | 15.4 ± 5.8 | 0.39 ± 0.4 | $4.4\times10^{-4}$ |
| *Post-hoc* | *N<TC,TR* | | | *N>TC,TR* | | | |

$T_{1S_1}$ and $T_{1S_2}$ were set as a constant value of 1 s. The post-hoc test was performed for $p < 0.05$. <: significantly smaller; >: significantly larger; not indicated: no significant difference.